Optics Letters

Observation of the bound states in the continuum supported by mode coupling in a terahertz metasurface

ZIJIAN CUI,[1] YUE WANG,[1,*] GUANGCHENG SUN,[1] WENSHUO CHEN,[1] KUANG ZHANG,[2] AND XINMEI WANG[1]

[1] *Key Laboratory of Ultrafast Photoelectric and Terahertz Science in Shaanxi, Xi'an University of Technology, 5 Jinhua South Road, Xi'an 710048, China*
[2] *Department of Microwave Engineering, Harbin Institute of Technology, 92 West Dazhi Street, Harbin 150001, China*
**wangyue2017@xaut.edu.cn*

Received 9 June 2023; revised 2 August 2023; accepted 16 August 2023; posted 16 August 2023; published 8 September 2023

Metasurface supporting bound states in the continuum (BIC) provides a unique approach for the realization of intense near-field enhancement and high quality factor (Q-factor) resonance, which promote the advancement of various applications. Here we experimentally demonstrate a Friedrich–Wintgen BIC based on the mode coupling in the terahertz metasurface, which produces BIC by the coupling of the LC mode and dipole mode resonances. The transition from ideal BIC to quasi-BIC is caused by the mismatch of the coupling, and the mode decay rate during this process is analyzed by temporal coupled mode theory. The Q-factor and the electric field enhancement of the quasi-BIC resonance are significantly increased, which provides enormous potential in sensing, nonlinear optics, and topological optics.

https://doi.org/10.1364/OL.497757

Rapid growth in the field of metasurfaces has led to significant advances in a wide range of application areas, such as electromagnetic wave tailoring [1], optical analog computing [2], and ultra-sensitive detection [3]. Among the research for metasurfaces, the pursuit of high quality factor (Q-factor) resonance has been an active topic, and of great important [4,5]. This is not only because the high Q-factor resonance provides significant local field enhancement, which makes more intense light–matter interaction [6], but also a resonance peak with narrow full-width at half-maximum (FWHM) benefits the sensing performance due to their shift is more evident when detecting [7–9]. To improve the Q-factor, a general method is reducing the gap width of the patterns [10]. A narrow gap effectively improves the Q-factor of the resonance. However, this will bring fabrication complexity and impose restrictions on design freedom. While this approach is intuitive, there is a limitation to further increasing the Q-factor due to the challenge of limited etching resolution.

Recently, the concept of the bound states in the continuum (BIC) has emerged as an effective means that enables the metasurfaces to achieve exceptionally high Q-factor resonance [11–13]. BICs are localized confined modes coexisting with extended modes, which result in an infinite Q-factor and lifetime. In theory, an ideal BIC exists in a system with no perturbations or in which the resonance modes have complete destructive interference, and is entirely decoupled from the far-field radiation. As a general physics phenomenon, BICs have enabled ultra-sharp resonance in various photonics systems [14–17]. In practice, however, a quasi-BIC with nonzero-linewidth resonance is preferred, which is at around an ideal BIC and has an observable resonance in the spectrum.

Quasi-BICs in the metasurfaces are mainly realized by two universal approaches. When the symmetry of the metasurface resonator unit is broken, asymmetric perturbations are introduced into the system, resulting in the leakage of symmetry-protected BIC [18,19]. Hence, the vanished radiative channel deviates from the steady state, leading to the coupling between the resonators and the incident [20–23]. Moreover, the BIC also can be transformed into quasi-BIC by mismatching the complete destructive interference between two resonant modes coupled to the same radiation channel [24,25]. The quasi-BIC presents a promising opportunity to further increase the Q-factor of the metasurface and significantly enhance the field intensity on the surface. Consequently, BIC metasurfaces have become a hot research topic and have been demonstrated across various platforms, indicating enormous potential for applications such as ultra-sensitive detection [26], nonlinear enhancement [27,28], and topological optical forces [29].

In this study, we propose and experimentally demonstrate a metasurface for terahertz frequencies that supports BIC or quasi-BIC resonance, which is associated with the geometry parameters of the metallic resonator units with in-plane symmetry. The quasi-BIC is formed by the mismatch of the coupling between inductive–capacitive (LC) modes and dipole modes generated by resonators. Additionally, we apply temporal coupled mode theory (TCMT) to explicate the underlying physics and discuss the variation of the decay rates in the transition process from ideal BIC to quasi-BIC. The Hamiltonian eigenvalues of the coupled system retrieve the resonance frequencies of the two modes during the coupling process. Moreover, the relations between the coupling deviation, Q-factor,

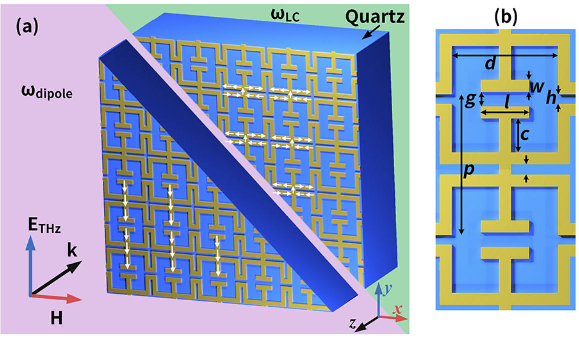

Fig. 1. (a) Schematic diagram of the metasurface sample composed of an interconnected metallic array. (b) Structure of the metasurface unit cell. For ideal BIC, $w = 5$ μm, $p = 58$ μm, $g = 5$ μm, $h = 4$ μm, $c = 14.5$ μm, $d = 44$ μm.

and electric field enhancement are discussed. The transmission spectra of the fabricated devices are measured by a terahertz time-domain spectrometer (THz-TDS), which reveals the impact of the material characteristics on the BIC resonance. Our results provide a convenient approach to achieve quasi-BIC resonance, which shows significant potential for applications in sensing and harmonic generation.

As shown in Fig. 1, the designed metasurface is composed of an interconnected metallic array on the quartz substrate. The incident electric field is along the y-axis. The geometric parameters of the metallic resonator unit are depicted in Fig. 1(b). The unit cell of the proposed metasurface is composed of T-shaped resonators and metallic loops between the adjacent unit cells. By carefully designing the geometric parameters of the resonator unit, the operating frequency and the coupling strength of the two modes can be tuned, supporting BIC and quasi-BIC without breaking the mirror symmetry.

When two resonance dips from different modes are designed to approach the same frequency, it will induce destructive interference, resulting in ideal BIC. To analyze the properties of BIC resonance and the transition from ideal BIC to quasi-BIC, we investigate the transmission characteristics of the designed metasurface under lossless conditions. The transmission spectra are shown in Fig. 2(a) when the gap g between the opposite T-shaped structures increases from 2 μm to 8 μm. As g increases, the linewidth of the transmission peak rapidly decreases, and the transmission peak disappears completely at $g = 5$ μm, showing the transition from quasi-BIC state to ideal BIC state. Subsequently, as g continues to increase, the transmission peak reappears, and the linewidth of the resonance peak gradually increases as the gap g deviates from the dimension of the ideal BIC condition. Similarly, the linewidth of the resonance peak gradually increases as the length l deviates from the design value, leading to an observable transmission peak in the spectrum accompanied by a gradual decrease in the Q value, as shown in Fig. 2(b).

To investigate the underlying physics of BIC, we calculate the electric field distributions at the resonance dip frequency for two different lengths, $l = 16$ μm and $l = 24$ μm, as indicated by the green and pink dots in Fig. 2(b). The electric field distributions are shown in Figs. 2(d)–2(g). Notably, both metal resonators with different lengths produce resonance dips at 1.247 THz. Moreover, the electric field distributions in Figs. 2(d) and 2(f) show similar characteristics, which are concentrated on the loops of adjacent resonator units, rather than the opposite T-shaped structure. The current will flow from the loops of adjacent cells, forming the capacitive part and inductive part of LC resonance. In contrast, the electric field concentrates on the vicinity of the opposite T-shaped structure at 1.067 THz when $l = 24$ μm, as shown in Fig. 2(e), forming a dipole mode resonance between adjacent unit cells, which is similar to the results in Fig. 2(g) (at 1.341 THz when $l = 16$ μm). These results indicate that the resonance frequency of the LC mode does not shift during the process of changing the length l. The variation of l only affects the dip frequency of the dipole mode. With the increase of l, redshift occurs continuously. The resonance dip in the gray shaded area of Fig. 2(b) originates from the LC mode, while the resonance dip originating from dipole resonance is marked by the red dashed ellipse. The resonance of the designed metasurface and the coupling can be intuitively equivalent to a two-port system, which includes the coupling between each mode as well as the coupling between incident and resonance. In general, the TCMT can be adopted to analyze the two-port coupled system [30,31],

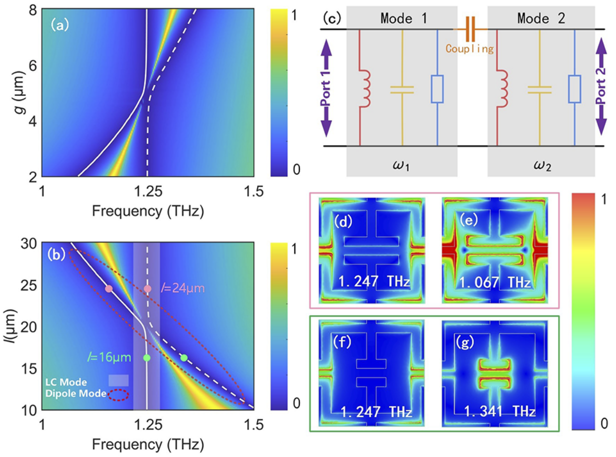

Fig. 2. (a) Transmission spectra of the designed metasurface as a function of the gap size g, and (b) gap length l. The white solid and dashed lines indicate the calculated resonance frequencies obtained from the eigenvalues of the Hamiltonian matrix, where $k = 0.01 \times 2\pi \times 10^{12}$. (c) Schematic of the two-port system with two coupled resonance modes. (d)–(g) Electric field distribution of the resonance dip at $l = 24$ μm and $l = 16$ μm.

$$\frac{\mathrm{d}a_i}{\mathrm{d}t} = jHa_i + Ks_{i+}, \tag{1}$$

where $a_i = [a_1, a_2]^{\mathsf{T}}$ is the positive frequency component of mode amplitude. Here H is Hamiltonian that represents the resonance frequency and the damping rate, and K represents the coupling coefficient between the resonance and port,

$$H = \begin{bmatrix} \omega_1 & k \\ k & \omega_2 \end{bmatrix} + j \begin{bmatrix} \gamma_1 & \gamma_{12} \\ \gamma_{21} & \gamma_2 \end{bmatrix}, \qquad K = \begin{bmatrix} k_{11} & k_{12} \\ k_{21} & k_{22} \end{bmatrix}, \tag{2}$$

where ω_1 and ω_2 are the dip frequencies of the two resonant modes, k represents the near-field coupling between the modes. Here γ_1 and γ_2 are the decay rates of the two modes, and $\gamma_{12} = \gamma_{21} = \sqrt{\gamma_1 \gamma_2}$ is the damping coupling coefficient. Here k_{ij} is the coupling coefficient between mode i and mode j. Importantly, by calculating the eigenvalues of the Hamiltonian matrix, we obtain the resonance frequencies of two modes with the influence of

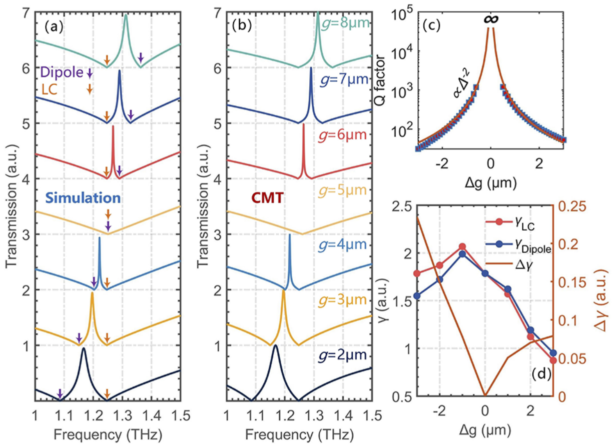

Fig. 3. (a) Simulations and (b) TCMT-calculated spectra while $g = 2, 3, 4, 5, 6, 7, 8\ \mu\mathrm{m}$. (c) Relation between the Q-value and the offset of the gap g. The Q-value approaches infinity at $\Delta g = 0$. (d) Decay rates of the LC and dipole modes with the variation of the gap g.

the coupling,

$$\omega_\pm = \frac{(\omega_1+\omega_2) - i(\gamma_1+\gamma_2)}{2} \pm \frac{\sqrt{[(\omega_1-\omega_2) - i(\gamma_1-\gamma_2)]^2 + 4\left(k - i\sqrt{\gamma_1\gamma_2}\right)^2}}{2}. \tag{3}$$

As shown in Figs. 2(a) and 2(b), the solid and dashed white lines represent the left and right branches of the resonance dip, respectively. It is worth noting that one eigenvalue of the H matrix becomes purely real with zero imaginary parts when $\omega_1 = \omega_2$, forming an ideal BIC. In this case, the coupling system satisfies the Friedrich–Wintgen condition: $k(\gamma_1 - \gamma_2) = \sqrt{\gamma_{12}\gamma_{21}}(\omega_1 - \omega_2)$ [32,33]. In this framework, the incident is transmitted through a resonator with two coupled resonance modes, and then transmitted to port 2. Based on energy conservation, the relationship between output s_{i-} and the incident s_{j+} is given by $s_{i-} = rs_{i+} + ts_{j-} + k_{ii}a_i + k_{ij}a_j$, where r and t are the direct reflection and transmission coefficient. The transmission can be calculated by $t_{ij} = s_{i-}/s_{j+}$, as shown in Fig. 3(b), which agrees well with the simulated results in Fig. 3(a).

It is worth noting that the transmission peak disappears at $g = 5\ \mu\mathrm{m}$, resulting in an ideal BIC. However, sharp transmission peaks are observed under other parameter conditions. Moreover, the dipole resonance gradually redshifts, as gap g decreases. Eventually, the corresponding resonance dip shifts from the right branch to the left branch. Based on the TCMT, the decay rates of the LC mode (γ_{LC}) and dipole mode (γ_{dipole}) of the metasurface are obtained, and the difference $\Delta\gamma$ between γ_{LC} and γ_{dipole} is calculated, as shown in Fig. 3(d). When $\Delta g = 0, \Delta\gamma = 0$. Hence, the BIC is forming at the avoided crossing point [34]. Moreover, the Q-value approaches infinity at this point, as shown in Fig. 3(c). The results show the quadratic relationship between the offset of the gap g and Q-value, as reported in many previous works [35]. Figure 4(a) shows the electric field distributions at BIC frequencies for $g = 2, 3, 4, 5, 6, 7$, and $8\ \mu\mathrm{m}$, respectively. It is obvious that the electric field is concentrated in the gap and becomes more intense as the gap g approaches $5\ \mu\mathrm{m}$. It should be noted that the electric field enhancement sharply decays at $g = 5\ \mu\mathrm{m}$ (ideal BIC condition). The maximum enhancement factor extracted from Fig. 4(b) provides a clearer representation of the variation in the electric field enhancement factor. A quadratic increase, analogous to the Q-values, is observed. However, the electric field enhancement is nearly disappearing when the ideal BIC condition is achieved, as the resonance modes of the metasurface are unable to couple with the incident. Notably, we obtain a more intense localized electric field in a large gap value g. This implies that electric field enhancement can be achieved using a simple fabrication process and increasing the spatial extent of light–matter interaction.

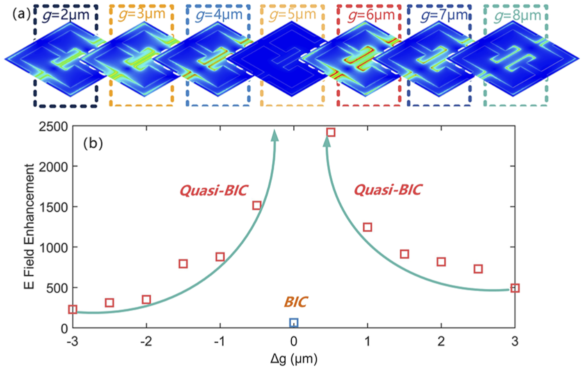

Fig. 4. (a) Electric field distribution of the BIC and quasi-BIC resonance. (b) Dependence of the electric field enhancement on the offset Δg.

We fabricated the devices with the gap length l of 16, 20, 24 μm. The 200 nm-thick gold layer is deposited on the quartz substrate, which is subsequently patterned into a periodic array of resonators by using ion beam etching. By using THz-TDS, the transmitted time-domain signals of the metasurface samples and the quartz reference are obtained. The transmission spectra are obtained by $|T(\omega)| = |E_{sample}(\omega)/E_{ref}(\omega)|$. Due to the material loss resulting from the metal resonators and the substrate, the intensity of quasi-BIC transmission peak decreases as shown in Fig. 5(a), which is in good agreement with the simulations shown in Fig. 5(b). Additionally, it is observed that despite offset from the ideal BIC condition being the same ($\Delta l = 4\ \mu\mathrm{m}$), the amplitudes and Q-factors of the resonant transmissions at 16

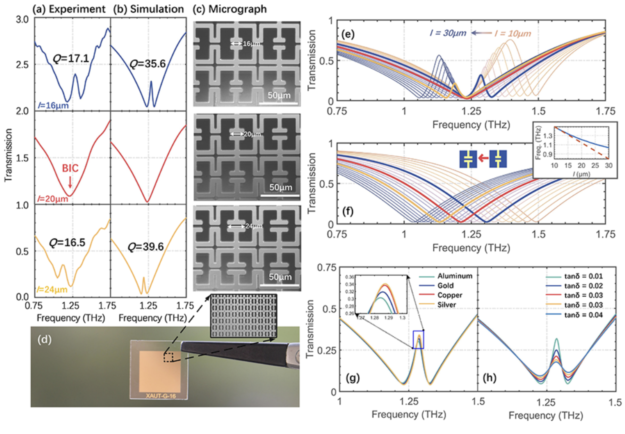

Fig. 5. (a) Measured and (b) simulated transmission spectra. (c) Micrograph and (d) photograph of the fabricated device. (e) Transmission spectra with the variation of the gap length l from 10 μm to 30 μm. (f) Transmission spectra of the individual dipole resonator as a function of the gap length l. (g) Impact of the resonator material and the loss tangent on the BIC transmission, respectively.

μm and 24 μm are different. This is evident in the transmission spectra as the gap length l varied from 10 μm to 30 μm, as shown in Fig. 5(e). The quasi-BIC transmission peaks exhibit larger variation as l increased from 10 μm to 20 μm, while the changes are relatively smaller as l increased from 20 μm to 30 μm. To get an in-depth understanding of this phenomenon, the simulations of the individual dipole resonator with varied gap length l are carried out, as depicted in Fig. 5(f). As the l increased, the resonance frequency of the dipole mode gradually redshifts, and the slope of the redshift continuously decreased, as shown in the inset of Fig. 5(f). Therefore, this leads to differences in the coupling with the LC mode, which in turn results in differences in the transmission characteristics. In addition, the experiment results reveal that material loss has an impact on the transmission spectrum. Therefore, we investigate the transmission properties of the designed metasurface using various metal materials while keeping the gap length l at 16 μm, as shown in Fig. 5(g). Compared with the lossless, the amplitude of the transmission peak has a significant attenuation. It can be observed from the zoomed inset in Fig. 5(g) that as the material conductivity increases, i.e., the loss decreases, the amplitude of the transmission peak rises ($\sigma_{Silver} > \sigma_{Copper} > \sigma_{Gold} > \sigma_{Aluminum}$). We also investigate how the loss of the dielectric substrate affects the transmission (gold resonator). As shown in Fig. 5(h), the amplitude of the transmission peak attenuates as the increase of dielectric loss tangent, and the resonance frequency has little effect.

In summary, we have experimentally investigated a terahertz metallic metasurface with in-plane mirror symmetry, which produces the LC mode and dipole mode resonance. The high-Q transmission peak and the intense electric field enhancement are obtained when the geometric parameter deviates from the ideal BIC condition, and the quadratic relationship with the offset is validated. Based on the TCMT, we have investigated the coupling between the intrinsic LC mode and dipole mode. When the coupling satisfies the Friedrich–Wintgen condition, two different intrinsic modes are tuned to the same frequency and destructive interference occurs. Further, the transmission peak of the quasi-BIC attenuates when inducing loss into the coupling system. This study provides an in-depth understanding of BIC based on metallic metasurfaces and presents a convenient approach to realize high-Q resonances, which have significant potential for applications in the fields of bio-optics, topological optics, and nonlinear optics.

Funding. National Natural Science Foundation of China (62275215, 61975163); Youth Innovation Team of Shaanxi Universities (21JP084); Key Research and Development Program of Shaanxi Province (2023GXLH-038); Natural Science Foundation of Shaanxi Province (2020JZ-48).

Disclosures. The authors declare no conflicts of interest.

Data availability. Data underlying the results presented in this paper may be obtained from the authors upon reasonable request.

REFERENCES

1. C. Liu, S. Wang, S. Zhang, Q. Cai, P. Wang, C. Tian, L. Zhou, Y. Wu, and Z. Tao, Adv. Photonics **3**, 056002 (2021).
2. D. Pan, L. Wan, M. Ouyang, W. Zhang, A. A. Potapov, W. Liu, Z. Liang, T. Feng, and Z. Li, Photonics Res. **9**, 1758 (2021).
3. J. Zhang, N. Mu, L. Liu, J. Xie, H. Feng, J. Yao, T. Chen, and W. Zhu, Biosens. Bioelectron. **185**, 113241 (2021).
4. Z. Gu, J. Chen, B. Gao, W. Wu, Z. Zhao, W. Cai, X. Zhang, M. Ren, and J. Xu, Opt. Lett. **47**, 1822 (2022).
5. W. Shi, J. Gu, X. Zhang, Q. Xu, J. Han, Q. Yang, L. Cong, and W. Zhang, Photonics Res. **10**, 810 (2022).
6. M. Amin, O. Siddiqui, H. Abutarboush, M. Farhat, and R. Ramzan, Carbon **176**, 580 (2021).
7. S. Romano, G. Zito, S. Torino, G. Calafiore, E. Penzo, G. Coppola, S. Cabrini, I. Rendina, and V. Mocella, Photonics Res. **6**, 726 (2018).
8. F. Yesilkoy, E. R. Arvelo, Y. Jahani, M. Liu, A. Tittl, V. Cevher, Y. Kivshar, and H. Altug, Nat. Photonics **13**, 390 (2019).
9. G. Zito, G. Sanità, B. Guilcapi Alulema, S. N. Lara Yépez, V. Lanzio, F. Riminucci, S. Cabrini, M. Moccia, C. Avitabile, A. Lamberti, V. Mocella, I. Rendina, and S. Romano, Nanophotonics **10**, 4279 (2021).
10. T. Dong, S. Li, and M. Manjappa, *et al.*, Adv. Funct. Mater. **31**, 2100463 (2021).
11. G. Yang, S. U. Dev, M. S. Allen, J. W. Allen, and H. Harutyunyan, Nano Lett. **22**, 2001 (2022).
12. L. Hu, B. Wang, Y. Guo, S. Du, J. Chen, J. Li, C. Gu, and L. Wang, Adv. Opt. Mater. **10**, 2200193 (2022).
13. X. Chen, Y. Zhang, G. Cai, J. Zhuo, K. Lai, and L. Ye, Nanophotonics **11**, 4537 (2022).
14. I.-C. Benea-Chelmus, S. Mason, M. L. Meretska, D. L. Elder, D. Kazakov, A. Shams-Ansari, L. R. Dalton, and F. Capasso, Nat. Commun. **13**, 3170 (2022).
15. I. A. Al-Ani, K. As' Ham, L. Huang, A. E. Miroshnichenko, and H. T. Hattori, Laser Photonics Rev. **15**, 2100240 (2021).
16. T. Shi, Z.-L. Deng, G. Geng, X. Zeng, Y. Zeng, G. Hu, A. Overvig, J. Li, C.-W. Qiu, A. Alù, Y. S. Kivshar, and X. Li, Nat. Commun. **13**, 4111 (2022).
17. G. Zito, S. Romano, S. Cabrini, G. Calafiore, A. C. De Luca, E. Penzo, and V. Mocella, Optica **6**, 1305 (2019).
18. D. R. Abujetas, N. van Hoof, S. ter Huurne, J. G. Rivas, and J. A. Sánchez-Gil, Optica **6**, 996 (2019).
19. S. Li, C. Zhou, T. Liu, and S. Xiao, Phys. Rev. A **100**, 063803 (2019).
20. T. Ma, J. Li, and Z. Luo, Opt. Laser Technol. **157**, 108745 (2023).
21. W. Liu, Z. Li, H. Cheng, and S. Chen, iScience **23**, 101868 (2020).
22. J. Wang, W. Liu, Z. Wei, H. Meng, H. Liu, J. Guo, M. Yang, Y. Song, L. Xiang, Z. Huang, H. Li, and F. Wang, Nanomaterials **11**, 2357 (2021).
23. H. M. Doeleman, F. Monticone, W. den Hollander, A. Alù, and A. F. Koenderink, Nat. Photonics **12**, 397 (2018).
24. X. Zhao, C. Chen, K. Kaj, I. Hammock, Y. Huang, R. D. Averitt, and X. Zhang, Optica **7**, 1548 (2020).
25. Z. Li, L. Zhou, Z. Liu, M. Panmai, S. Li, J. Liu, and S. Lan, ACS Photonics **10**, 206 (2023).
26. Y. K. Srivastava, R. T. Ako, M. Gupta, M. Bhaskaran, S. Sriram, and R. Singh, Appl. Phys. Lett. **115**, 151105 (2019).
27. C. Fang, Q. Yang, Q. Yuan, L. Gu, X. Gan, Y. Shao, Y. Liu, G. Han, and Y. Hao, Laser Photonics Rev. **16**, 2100498 (2022).
28. Z. Liu, Y. Xu, Y. Lin, J. Xiang, T. Feng, Q. Cao, J. Li, S. Lan, and J. Liu, Phys. Rev. Lett. **123**, 253901 (2019).
29. S. Yang, C. Hong, Y. Jiang, and J. C. Ndukaife, ACS Photonics **8**, 1961 (2021).
30. W. Suh, Z. Wang, and S. Fan, IEEE J. Quantum Electron. **40**, 1511 (2004).
31. S.-Y. Cho, J. Sun, A. C. Overvig, A. Alù, and W. Zhou, ACS Photonics **9**, 3592 (2022).
32. M. Kang, S. Zhang, M. Xiao, and H. Xu, Phys. Rev. Lett. **126**, 117402 (2021).
33. H. Friedrich and D. Wintgen, Phys. Rev. A **32**, 3231 (1985).
34. C. Schiattarella, G. Sanità, B. G. Alulema, V. Lanzio, S. Cabrini, A. Lamberti, I. Rendina, V. Mocella, G. Zito, and S. Romano, Biosens. Bioelectron.: X **12**, 100262 (2022).
35. K. Koshelev, S. Lepeshov, M. Liu, A. Bogdanov, and Y. Kivshar, Phys. Rev. Lett. **121**, 193903 (2018).